**OPEN**

Correspondence and
requests for materials
should be addressed to
J.Y. (jiandong.ye@
anu.edu.au) or K.L.T.
(eleteokl@nus.edu.sg).

# Spin-polarized Wide Electron Slabs in Functionally Graded Polar Oxide Heterostructures

Jiandong Ye[1,2], Sze Ter Lim[3], Michel Bosman[4], Shulin Gu[1], Youdou Zheng[1], Hark Hoe Tan[2], Chennupati Jagadish[2], Xiaowei Sun[5] & Kie Leong Teo[3]

[1]School of Electronics Science and Engineering, Nanjing University, 210093 (PR China), [2]Department of Electronic Materials Engineering, Research School of Physics and Engineering, The Australia National University, Canberra, 0200, (Australia), [3]Department of Electrical and Computer Engineering, National University of Singapore, 117576 (Singapore), [4]Institute of Materials Research and Engineering, A-STAR (Agency for Science, Technology, and Research), 3 Research Link, 117602 (Singapore), [5]School of Electrical & Electronic Engineering, Nanyang Technological University, Nanyang Avenue, 639798 (Singapore).

We report on the high mobility wide electron slabs with enhanced correlation effects by tailoring the polarization effects in a functionally graded ZnMgO/ZnO heterostructures. The characteristics of three-dimensional (3D) spreading electrons are evidenced by the capacitance-voltage profiling and the quantization of 3D Fermi surface in magneto-transport measurements. Despite the weak spin-orbit interaction, such electron slabs are spin-polarized with a large zero-field spin splitting energy, which is induced by the carrier-mediated ferromagnetism. Our results suggest that the vast majority of electrons are localized at the surface magnetic moment which does not allow spin manipulations, and only in the region visited by the itinerant carriers that the ferromagnetic exchange interactions via coupling to the surface local moments contribute to the spin transport. The host ferromagnetism is likely due to the formation of Zn cation vacancies on the surface regime induced by the stabilization mechanism and strain-relaxation in ZnMgO polar ionic surface.

O wing to the richness of their intrinsic properties, transition metal oxides can bring novel functionalities to modern electronics. Recent technical advances in the fabrication of atomically abrupt oxide interface enable the formation of high mobility two-dimensional electron gases (2DEG) and trigger intense research of unusual electronic properties in deliberately designed oxide structures[1–5]. In particular, the emerging phenomena of metal-insulator transition and quantum Hall ferromagnet have been observed in a diluted ZnMgO/ZnO strongly correlated 2DEG[1,6]. Of interest to high frequency device application, it is essential to dilute the carrier density in device channel because that the build-up of non-equilibrium polar optical phonons will limit the high-field velocity of carriers in high density 2DEG. It is also expected that the reduction of charge carrier density will further increase the correlation effects, resulting in enhancements of the electron mass and spin susceptibility[1]. Spreading carriers into a wide compositionally graded heterostructure is an effective mean to dilute the carrier density, as demonstrated in the graded AlGaN/GaN and graded AlGaAs/GaAs wide parabolic quantum wells[7–9]. Such a low density three-dimensional (3D) electron slab is also a ubiquitous paradigm in solid-state physics and quantum chemistry[10]. If the spin degree of freedom is incorporated, spin physics as a new frontier will offer more intriguing studies in spintronics. It is also promising to develop novel spintronic devices by utilizing the desirable spin-polarization feature of high mobility electron system[11]. Recently, the compositionally graded ZnMgO structures have been utilized to reduce the internal electric field of quantum wells and enhance the surface Schottky barrier[12–13]. Here, we explore the polarization effects in a functionally graded pseudomorphic ZnMgO/ZnO heterostructure. By tailoring the bandgap and polarization effects, a diluted three-dimensional electron slab (3DES) can be achieved without compromising the high mobility characteristics. The intriguing phenomena of spin-polarization and carrier-mediated ferromagnetism in such a strongly correlated electron system have been investigated. The formation mechanism and quantum transport of 3DES are examined in terms of band structure and polarization effect.

1

## Results

**Tailoring the polarization effects in functionally graded polar oxides.** A compositional grading feature in ZnMgO layer will result in a non-vanishing divergence of polarization. It is well understood from the theory of dipole engineering established by D. Jena et al[7–8,14]. Figure 1 (a) shows the polarization field in the [0001] direction for a linearly graded ZnMgO/ZnO heterostructure studied in this work. The distribution of polarization dipoles and the resultant carriers are depicted schematically in Figure 1 (b) and (c), respectively. For a compressively strained ZnMgO layer, both spontaneous polarization and piezoelectric polarization should be taken into account while in a completely relaxed thick ZnO underlayer, the spontaneous polarization is only considered. In Fig. 1 (b), each unit cell is assumed to contain a charge dipole due to spatial separation of centroids of the electron clouds and the nuclei. The dipoles sheets in each unit cell neutralize each other in bulk ZnO. However, the strength of the dipole changes with increasing Mg composition, breaking the local charge neutrality in the ZnMgO layer. To visualize the microscopic landscape of polarization effect, we divide the $Zn_{1-x}Mg_xO$ layer into $N$ unit cells with a Mg composition linearly increasing from the interface ($z=z_0$) to the top surface ($z = 0$). The unit number $N$ is equal to $d/c$, where $d$ is the thickness of graded layer, and c is the length of a unit cell. For the $i^{th}$ unit cell, Mg composition is $\frac{N-i}{N-1}z_0$, and the unbalanced bound sheet charge is equal to $\left|P^i_{SP+PE}/q\right|$ and $-\left|P^i_{SP+PE}/q\right|$ at the upper and lower surface, respectively. Due to the gradient polarization discontinuity $\Delta P (= |\Delta P_{SP}| - |P_{PE}|) < 0$[4], the unbalanced net bound charges are positive with its sheet density of $\left(P^i_{SP+PE} - P^{i+1}_{SP+PE}\right)/q$ at the interface between the $i$th and $(i+1)$th unit cells. As a result, the bound positive polarization charges are spread throughout the linearly graded layer with a volume density of $N_{D\pi} = \nabla P = \sigma_\pi/dq$[7]. Consequently, these fixed positive charges will attract mobile electrons to satisfy the Poisson's equation and local charge neutrality in the bulk. Thus, gradient polarization magnitude introduces a three-dimensional mobile electron slab (3DES).

**Composition gradient in ZnMgO/ZnO heterostructure.** In this work, the polarization gradient is experimentally realized by utilizing the compositional pulling effect in ZnMgO/ZnO heterostructure grown on sapphire under thermal equilibrium conditions

by metal-organic vapor phase epitaxy (MOVPE) technique[15]. The details are given in the Method section. The single heterostructure (sample A) consists of a $Zn_{1-x}Mg_xO$ (75 nm) on ZnO template with $x = 0.18$ at the topmost surface, while the double heterostructure (sample B) has a sandwich feature: graded-$Zn_{0.8}Mg_{0.2}O$ (60 nm)/ ZnO (30 nm)/graded-$Zn_{0.85}Mg_{0.15}O$ (90 nm). Figure 2 (a) shows a cross-sectional image of sample B obtained by high-angle annular dark-field cross-sectional scanning transmission electron microscopy. The sandwiched ZnO layer appears as bright because the heavier $Zn^{2+}$ ions appear brighter than the $Mg^{2+}$ ions. The atomic lattice in both ZnMgO and ZnO layers is clearly seen (right enlarged image in Fig. 2 (a)), indicative of state-of-the-art epitaxial heterostructure formed. Fig. 2 (b) shows energy-dispersive X-ray (EDX) chemical maps of Mg and Zn, and as well as monochromated low-loss electron energy-loss spectroscopy (EELS) data. The contrast in the maps illustrates the composition distribution of Zn and Mg in the heterostructure and the spatially resolved EELS spectra exhibit a stepwise absorption feature resulting from the electronic bandgap onset. The EELS spectra are displayed at 5 nm intervals, with ZnO region as marked by red lines. The extracted bandgap profile at the right of Fig. 2 (b) was taken from all 1nm-spaced EELS spectra. The profile shows a linear bandgap-energy reduction, which is consistent with the Zn and Mg distributions of ZnMgO layers. This indicates that the gradient distribution of Mg in ZnMgO layers has been achieved. This compositional gradient phenomenon in ZnMgO layer is known as compositional pulling or lattice latching effect, which is related to the misfit strain in the films[16–17]. From the viewpoint of thermodynamics, the biaxial compressive strain will pull the Mg adatoms from the growing front surface of ZnMgO in the initial stage to reduce the deformation energy. As growth continues, a graded strain reduction allows the subsequent deposition of a ZnMgO layer with high $x$. Due to the gradual distribution of strain throughout the whole ZnMgO layer and not accumulated at the sharp interface, the ZnMgO layer can grow coherently in the critical range without generating new misfit dislocations. The slope of grading can be tuned by various thermodynamic growth conditions such as temperature and Mg/Zn gas-phase mole ratio[18].

**Strain evolution and polarity stabilization in graded ZnMgO layer.** The piezoelectric polarization field is sensitive to the strain evolution in graded ZnMgO layer, which can be examined by means of high resolution x-ray diffraction. Figure 3 (a) and (b)
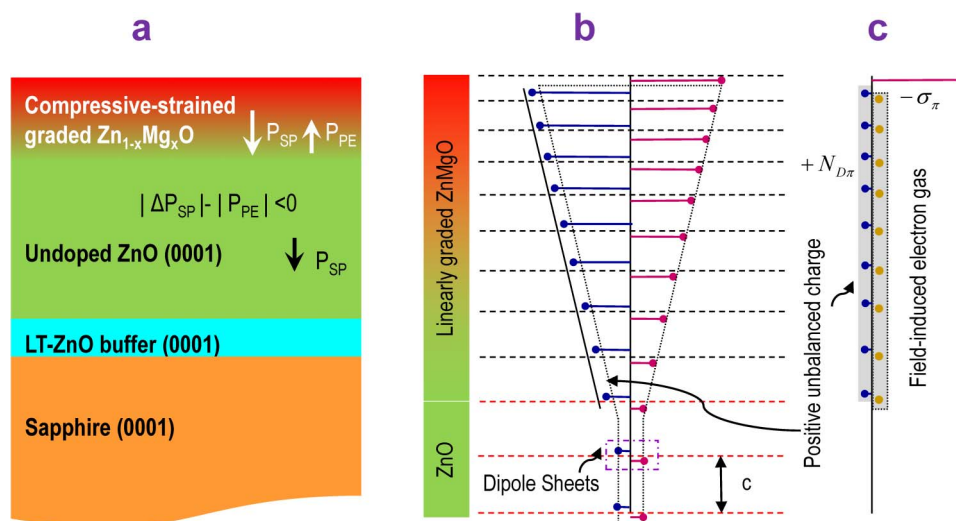


**Figure 1 | (a) Polarization field directions, (b) schematic distribution of polarization dipole and (c) distribution of resultant carriers in the linearly graded ZnMgO/ZnO heterostructure in the [0001] orientation.** $P_{SP}$ and $P_{PB}$ represent the spontaneous and piezoelectric polarizations, respectively. The parameter c is the lattice constant, $\sigma_\pi$ is the polarization-induced charges on top of the surface and $N_{D\pi}$ is the sheet density of positive unbalanced polarization charges.
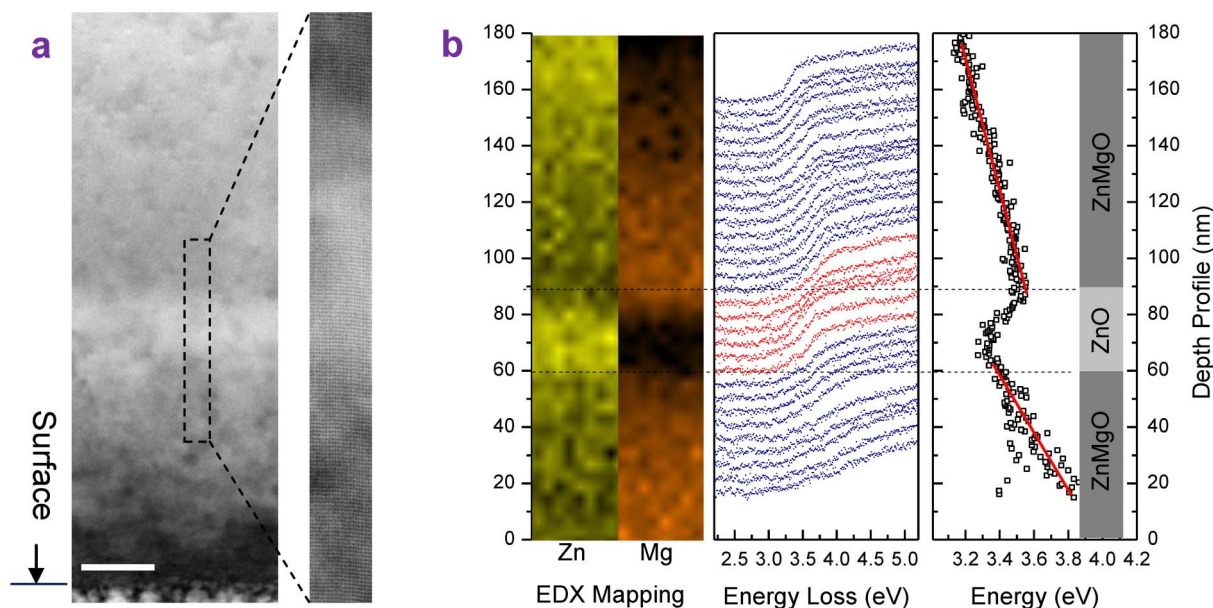
Figure 2 | (a) Cross-sectional STEM HAADF image and the corresponding higher magnification image of the boxed region; (b) (left to right) EDX chemical maps with projected Mg and Zn, monochromated low-loss EELS spectra and the extracted bandgap energy profile of ZnMgO/ZnO/ZnMgO double heterostructures (sample B).

illustrate the reciprocal-space maps (RSMs) recorded in the vicinity of (105) asymmetric reflection of ZnMgO/ZnO heterostructures of sample A and B, respectively. In both samples, identical reciprocal coordinate $q_x$ are obtained for both ZnMgO and ZnO template which indicate that ZnMgO barrier layers are coherently strained to the underlying ZnO layers. The lattice constant of the pseudomorphic ZnMgO barrier along the c-axis decreases less gradually than the relaxed films, suggesting that the alloying barriers suffer from the in-plane compressive (out-of-plane tensile) strain[19]. The elongated and broadened reciprocal lattice point of ZnMgO along $q_z$ vector indicates a gradual decrease of the lattice constant along c-axis, clearly exhibiting the presence of Mg composition gradient.

We employed X-ray photoemission spectroscopy (XPS) to probe the chemical and electronic nature of ZnMgO surface. The shape of valence band (VB) XPS in Figure 4 (a) clearly exhibits Zn-polarity, in which O 2p valence band states are distinguished[20]. It is known that ZnMgO epilayers exhibit higher spontaneous polarization effects than ZnO. Due to large electronegativity of oxygen, the polar surfaces are electrostatically unstable, and the surface reconstruction or hydroxide absorption is considered crucial to stabilize the polar surface[21–23]. In checking for O 1s core-level spectrum, only one dominant peak at 531.00 eV was observed in Fig. 4(b) due to oxygen in the bulk, and thereby the absorbed OH groups were not obviously present in such clean surface. Thus, the surface reconstruction with formation of structural defects could be the dominant stabilization mechanism. The analysis of XPS indicates that the atomic ratio of [O]/[Zn+Mg] on Zn-polar ZnMgO epilayer is 49.70/48.84, slightly deviated from the stoichiometry. The modification of the surface stoichiometry for the stability of (0001)-Zn surface is also related to the redistribution of the surface charges through the formation of O-terminated defects. The atomic force microscopic image in Figure 4(c) exhibited the triangular jagged step edges and tiny pits were dominant on the surface graded ZnMgO layer and the mean surface roughness is only 0.42 nm over 3 μm×3 μm area. These triangular shaped features are similar to those observed by Dulub et al[21], which are not present on the O-polar or nonpolar faces. In fact,
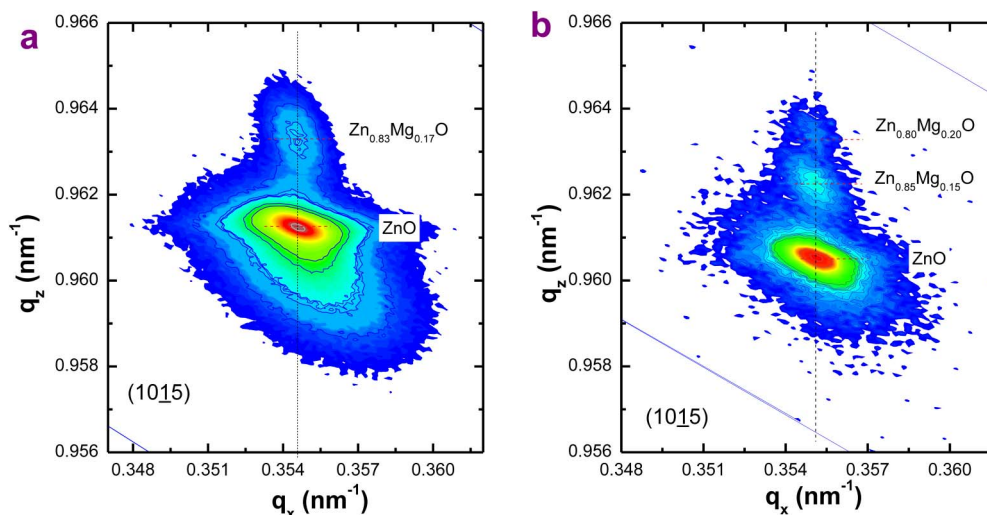


Figure 3 | (105) asymmetric RSMs of sample A (a) and sample B (b).
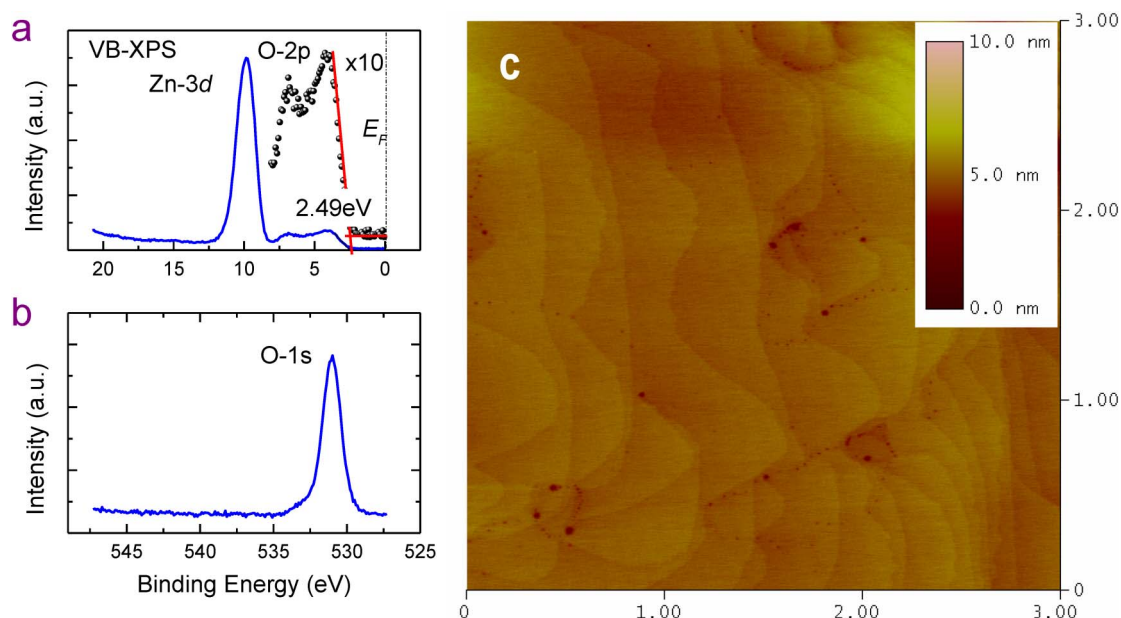
**Figure 4** | (a) The valance-band and (b) O 1s core-level x-ray photoelectron spectrum of sample A calibrated by carbon 1s (284.6 eV); (c) AFM images of (a) ZnMgO/ZnO double heterostructure (sample B).

during the step-flow growth under thermal equilibrium, the different growth speed is determined by different dangling bond densities at two kinds of step edges, leading to the jagged structures. The theoretical calculations and experimental results suggests that these step edges are O-terminated and thereby result in the overall decrease of the surface Zn concentration, which in turn build in a net-electric field to compensate the electrostatic surface instability[21–22]. On the other hand, the lattice-mismatch induced compressive strain in ZnMgO will tend to relax and give priority to the formation of tiny pits at the step edges of terraces. These pits are also considered to be clusters of negative charged Zn vacancies with O-terminated hexagonal cavities[23]. Therefore, the formation of structural defects Zn vacancies or even vacancy clusters are energetically favored and abundant on the surface regime.

**Polarization charge distribution and carrier profile of 3DES.** The polarization tailoring effect is verified by performing self-consistent Poisson and Schrodinger band calculations based on the surface charge model[24]. Figure 5 (a) and (b) show the calculated band diagrams and charge profiles at zero bias for both structures, and the real carrier profiles of samples derived from capacitance-voltage (C-V) measurements. The surface potential is determined to be 1.2 eV by VB-XPS in Fig. 4 (a), where the Fermi level is located at energy level of 2.49 eV above the maximum of valence-band and the corresponding bandgap of ZnMgO on the surface is 3.69 eV. The polarization constants used in the calculation are obtained from Ref.[25]. Taking both the spontaneous and piezoelectric polarization effects into account, the polarization discontinuity in a coherently strained ZnMgO is expressed as $P^{SP+PE}(x) = 0.029x(C/m)$[26]. For a linear gradient from ZnO to ZnMgO over length $d$ with $x(z) = x_0 z / d$ ($x_0$ is the Mg composition on the topmost surface), the volume density of itinerant carriers is given as $n_{3D} = N_{D\pi} = 0.029 x_0 / d$. It is found that the calculated carrier profile coincide well with those derived from C-V profiling. As expected, mobile carriers are accumulated within the graded barrier layer with a depletion layer $d_{depl}$ near the surface due to upward band bending. The resultant carrier sheet density is approximated to be $n_{3D} \times (d - d_{depl})$ with sheet density of $1.48 \times 10^{12}$ and $3.89 \times 10^{12}$ cm$^{-2}$ for samples A and B, respectively. It is noted that the spreading widths of electron slabs are larger than the thermal de-Broglie wavelength

($\lambda_{dB} = h / \sqrt{2m*k_B T} \approx 21$ nm at 300 K) or Fermi wavelength ($\lambda = 2\pi/k_F \approx 26$ nm) for the given carrier density of $n_{3D} = 4.77 \times 10^{17} cm^{-3}$ in sample A. The electronic system here is therefore expected to have a 3D single particle energy spectrum, and the carriers act just like bulk doped electrons but with high mobility.

**Quantum transport of spin-polarized high mobility carriers.** Figure 6 shows the temperature dependent Hall effect data for both samples A and B and a ZnO template for reference. At high temperature, the differences in sheet carrier concentration and mobility are not well distinguished between heterostructures and ZnO template because the parallel conduction path served by the ZnO underlayer dominate the Hall signal. As a result, a huge deviation of $n_s$ obtained by the overall Hall data ($1.16 \times 10^{14}$ cm$^{-2}$) and C-V profiling ($1.48 \times 10^{12}$ cm$^{-2}$) is observed. Once at low temperature, the parallel conduction path is greatly suppressed because most of electrons are frozen onto their parent donors in ZnO underlayer, and the resultant concentration decreases greatly and approaches to the real density of electron gas housed in the graded ZnMgO layer, as seen in Fig. 5 (b). We note that the parallel conduction path from ZnO underlayer is not completely suppressed, and thus, the carrier concentration of 3DES determined by the Hall Effect is still overestimated while the mobility is underestimated. Alternatively, we have performed the cyclotron resonance measurements by using terahertz time-domain magneto-spectroscopy at 1.4 K. Since the terahertz conductivity is a local probe of carrier dynamics[27], this may provide us more accurate information on the real 3DES. Our results show that for sample A, the carrier concentration, effective mass and mobility of the electrons are obtained to be: $n_s = 1.8 \times 10^{12} cm^{-2}$; $m^* = 0.33 m_e$; $\mu = 3500 \, cm^2/Vs$. We note that the carrier mobility for the polarization-doped 3DES is more than two orders of magnitude improvement as compared to undoped ZnO template. The low mobility of only 12 cm$^2$/Vs for undoped ZnO is caused by ionized impurity scattering. While in 3DES case, the carriers spreading in a wide graded ZnMgO layer are ionized by the non-vanishing polarization field. Owing to the removal of ionized impurity scattering, no sign of electron freeze-out at low temperature is observed and thus gives rise to metallic state of 3DES with high mobility. The main limitation mechanism in 3DES is alloy disorder
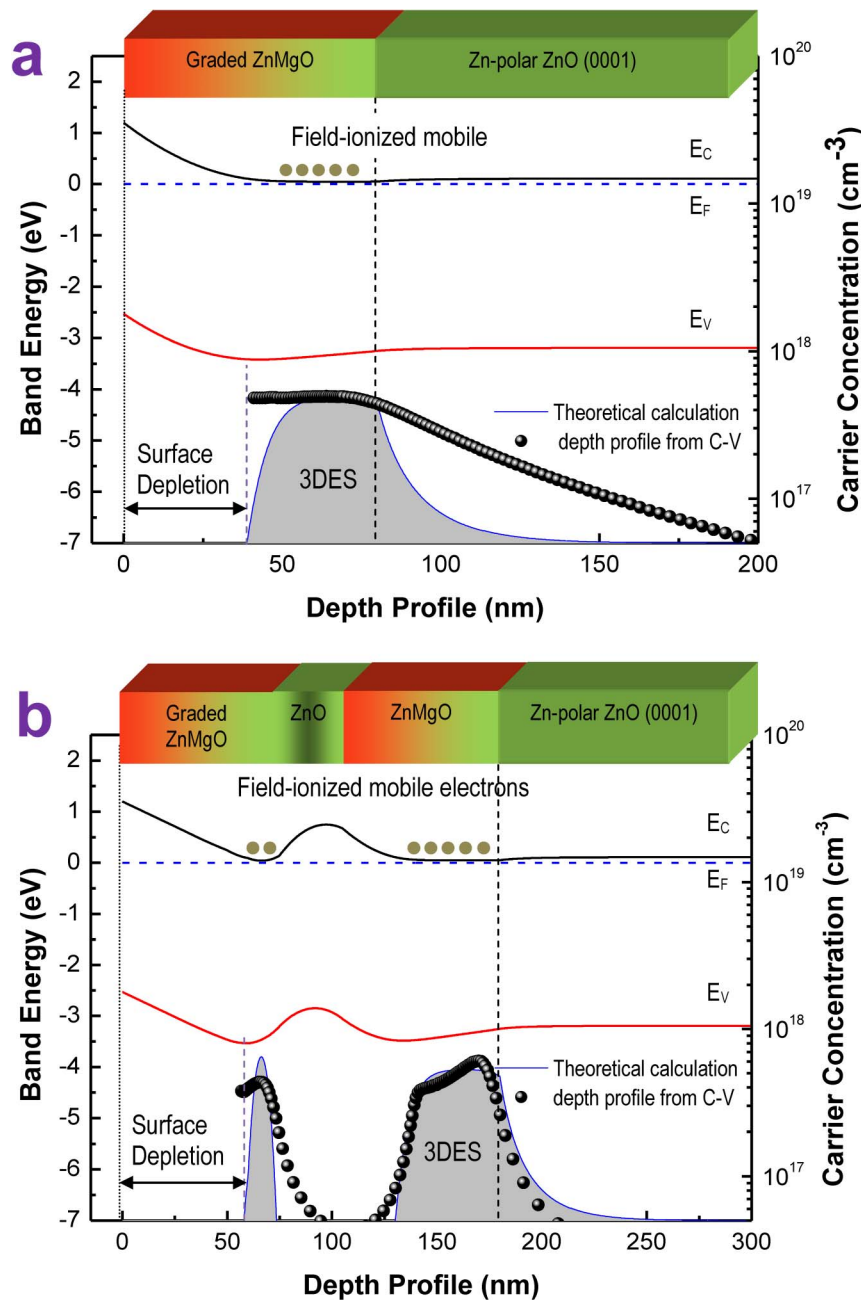
**Figure 5 | The calculated band diagrams and charge profiles at zero bias and carrier depth profile derived from C-V measurements for (a) sample A and (b) sample B.**

scattering, since the entire electron system completely resides in the graded ZnMgO layer[14]. As the volume density of the 3DES is diluted, the electron system can no longer fully screen the random disordered alloy potential, leading to the increased possibility of alloying disorder scattering. Furthermore, random spatial electric dipole moment due to the replacement of Zn by Mg atoms will result in a non-periodic electronic potential[28], thereby enhancing the dipole scattering of mobile electrons.

Next, we turn to the quantum transport properties of the 3DES. If ignoring the quantum electron-electron correlation effects, the 3DES investigated here has 3D Landau-level spectrum without variations of the density of states due to dimensional quantization across the spreading layer, as confirmed by CV profiling. However, below a certain temperature, the characteristic coherent length ($l_T = \sqrt{D\hbar/k_B T}$ $\approx 160\ nm$) for coherent transport is larger than the electron spreading width, and thus, the system becomes 2D for coherent phenomena in

the diffusive transport[29] ($D = v_F l$ is the diffusion coefficient along the magnetic field, $l = v_F \tau = 55.7\ nm$ is the mean free path for sample A). Figure 7 shows the angular-dependent magnetoresistance ($R_{xx}$) and Hall resistance ($R_{xy}$) as a function of magnetic field for sample A. When the magnetic field is perpendicular to the sample surface ($z//B, \theta = 0^0$ where $z$ is the growth direction), the structure of $R_{xx}$ and $R_{xy}$ resemble the Shubnikov-de Haas (SdH) oscillation and quantum Hall effect (QHE) for a 2D electron system. Above $\sim3$ T, well-resolved SdH oscillations and quantum Hall plateaus are observed, and the minima of $\rho_{xx}$ coincide well with the quantized Hall resistivity ($\rho_{xy}$) plateaus of $h/(vq^2)$, where $v$ is the Landau filling index. However, compared to the conventional QHE in 2DEG, neither the steps of $R_{xy}$ plateaus are completely flat nor the minima of $R_{xx}$ are very deep. This is due to the energy gap that is not yet fully developed in a finite magnetic field[27]. The negative parabolic magnetoresistance characteristic is observed at low field. It is related to the weak localization and
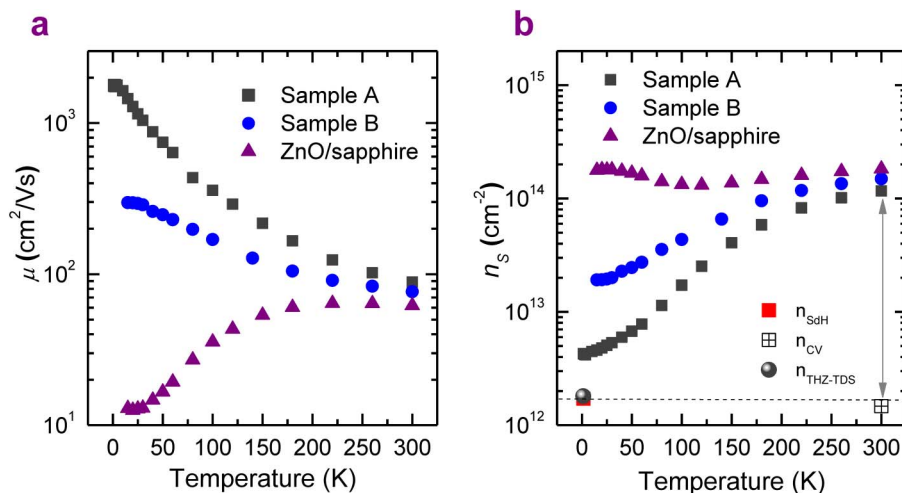
**Figure 6 | (a) Mobility and (b) sheet carrier concentration of ZnMgO/ZnO heterostructures (samples A and B) as well as the reference ZnO template.**

electron-electron interaction effects, which only occur in the coherent diffusive transport regime[30]. By rotating the magnetic field away from the perpendicular orientation, the minima in $R_{xx}$ are strongly suppressed. With the magnetic field parallel to the sample surface ($z \perp B, \theta = 90°$), the SdH oscillation can still be observed to start with an onset at higher field, which unambiguously implies the quantization of three-dimensional bulk Fermi surface. However, the in-plane oscillation amplitude decreased greatly, which could be ascribed to the finite ratio of the electron spreading width with respect to the magnetic length ($l_0 = \sqrt{\hbar/eB}$). The similar features of SdH oscillations under in-plane magnetic field have also been observed in AlGaAs/GaAs wide parabolic quantum well and heavily doped GaAs layer[29,31].

The theoretical expression of the envelope function of the SdH oscillation in 3D case can be given as[31]

$$\frac{R_{xx} - R_0}{R_0} = \frac{2}{5} \left( \frac{\hbar \omega_c}{2E_{F(3D)}} \right)^{1/2} \frac{A_T}{\sinh A_T} \exp\left( -\frac{\pi}{\omega_c \tau} \right) \cos\left( \frac{E_{F(3D)}}{\hbar \omega_c} - \frac{\pi}{4} \right)$$

Where $A_T = (2\pi^2 k_B T)/(\hbar \omega_c)$, $E_{F(3D)} = \frac{\hbar^2}{2m^*}(3\pi^2 n_{3d})^{\frac{2}{3}}$ is the Fermi

energies of 3D states, $\omega_c = (eB)/(mc)$ is the cyclotron frequency, $m$ is the electron effective mass, $\tau$ is the quantum scattering time, and $R_0$ represents the classical resistance in zero magnetic fields. When the high mobility system is at extreme low temperature of 1.4 K, the magnetoresistance exhibited a weakly modulated ($\sim B^{1/2}$) dependence of $\cos\left( \frac{E_{F(3D)}}{\hbar \omega_c} - \frac{\pi}{4} \right)$, and the period of the oscillatory cosine term yields the carrier density. We employed the standard Fast Fourier Transform (FFT) method to extract the periodicity of SdH oscillatory component and the FFT power spectrum is shown in Fig. 7 (b). Two peaks are clearly resolved with their locations at $f_1 = 51.92$ T and $f_2 = 19.26$ T, together with a shoulder peak on the left side of $f_1$ peak. The peak fitting result indicates that the shoulder peak is superimposed by the second harmonic peak $2f_2$ and the dominant peak $f_1$. If we assume that the two FFT peaks arise from the population of two subbands, the sheet carrier concentration is then given as $n_s = 2e(f_1 + f_2)/\hbar = 3.44 \times 10^{12}$ cm$^{-2}$, while if considering the spin-polarized Fermi surface, the value is $n_s = e(f_1 + f_2)/\hbar = 1.72 \times 10^{12}$ cm$^{-2}$. The latter value agrees well with the concentrations
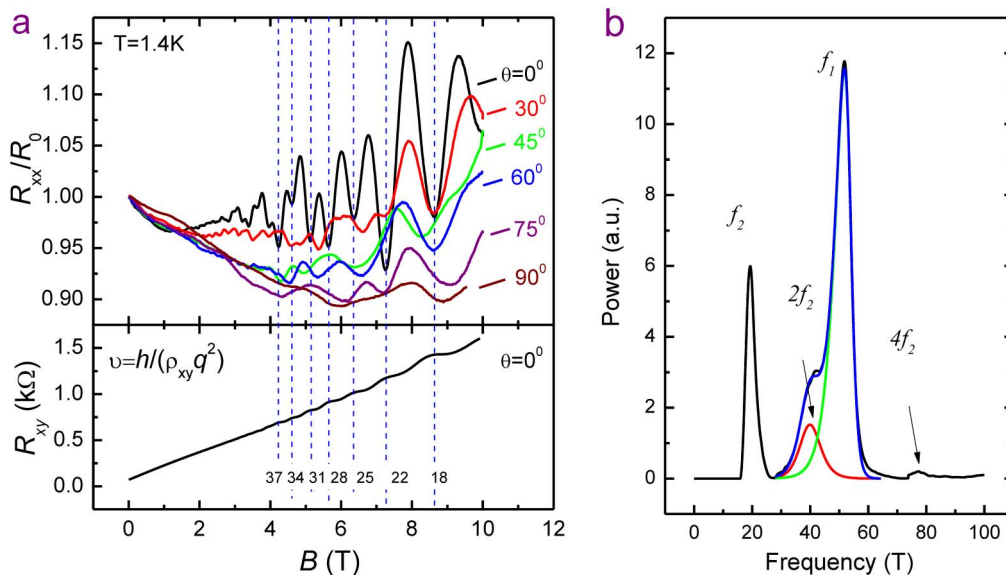


**Figure 7 | (a) Angular-dependent normalized magnetoresistance $R_{xx}/R_0$ versus $B$ and Hall resistivity $R_{xy}$ of sample A as a function of magnetic field ($z // B$, $\theta = 0°$) at 1.4 K; (b) FFT power spectrum of $R_{xx}$ versus $B$ at 1.4 K.**

derived by means of capacitance-voltage ($1.48 \times 10^{12}$ cm$^{-2}$ at RT) as well as cyclotron resonance ($1.8 \times 10^{12}$ cm$^{-2}$ at 1.4 K). Thus, the resultant volume carrier concentration ($n_{3d}$) is calculated be $4.77 \times 10^{17}$ cm$^{-3}$. Correspondingly, we can conclude that such diluted 3DES are partially spin polarized with spin polarization degree $\zeta$ ($\equiv |n_\uparrow - n_\downarrow|/n$) of 0.46, and a large zero-field spin-splitting energy $\Delta E (= 2\pi\hbar^2(n_\uparrow - n_\downarrow)/m^*)$ of 11.5 meV. Here $n_\uparrow$ and $n_\downarrow$ are the spin-up and spin-down carrier densities and $m^* = 0.33m_e$.

## Discussion

In the framework of Landau's Fermi liquid approach, the carrier-carrier interaction effects can be described using a dimensionless Wigner-Seitz parameter $r_s$, which is defined as the ratio of Coulomb interaction to Fermi energy. The $r_s$ value has a strong dependence on carrier concentration with the relationship given as $\frac{4}{3}\pi a_B^3 r_s^3 = n_{3d}$ in 3D case[32]. Here, $a_B = (\varepsilon/m_b)a_b = 1.54$ nm, which gives the effective Bohr radius with dielectric constant of $\varepsilon = 8.45$ and effective mass of conduction-band electron ($m_b = 0.29m_e$). Given the volume carrier concentration of $n_{3d} = 4.77 \times 10^{17}$ cm$^{-2}$, $r_s$ in sample A is 6.25. We note that it is rather difficult to achieve high $r_s$ value while still maintaining a high mobility in other semiconductor materials. Due to very small lattice mismatch, the pseudomorphic growth of $Zn_{0.8}Mg_{0.2}O$ on ZnO can be achieved with critical thickness up to 700 nm[19]. Thus, it is possible to further tune down the gradient of Mg composition in a wider thickness range and the polarization-induced charge density of high mobility 3DES can be diluted lower than $10^{16}$ cm$^{-3}$. In this situation, the corresponding value of $r_s > 22$ can be reached, and new physics such as metal-insulator transition or even quantum Hall ferromagnetic states can possibly be observed.

Knowing the interaction effects of carriers in diluted 3DES, we can now re-examine the feature of huge spin splitting energy of 11.5 meV in such intrinsic ZnMgO/ZnO system. The well-known Rashba spin-orbital coupling (SOC) effect due to inversion asymmetry are usually responsible for the zero-spin splitting phenomenon observed in AlGaAs/GaAs material systems. However, the SOC coefficient is very small in ZnO (about 1.1 meV Å)[33], and thus, it cannot explain our result. In fact, as the magnetic field is applied parallel to the surface of sample A, the Lorenz force and weak localization due to orbital effects are eliminated, and the distinct negative magnetoresistance is observed. This strongly suggests the inherent magnetic

order of 3DES[34]. The scenario of magnetic impurity induced spin-polarization can be ruled out because no magnetic impurities are detected by SIMS measurement within its detection sensitivity. Thus, the spin polarization observed in the magneto-transport is due to the ferromagnetic phase of electrons in 3DES, similar to the observations in 2DEG confined in non-magnetic polar oxides ($LaAlO_3/SrTiO_3$) heterostructures[35]. Theoretical study has predicted an itinerant 3DES will undergo a transition to a ferromagnetic phase in the limit of a large ratio of Columbic to kinetic energy ($r_s > 50$)[36]. By comparison, $r_s$ for 3DES investigated here is not large enough to induce the quantum Hall ferromagnetic phase, and therefore, we infer that the spin polarization is originated not only from the intrinsic electron-electron interaction but also includes other effects.

Figure 8(a) shows the magnetic hysteresis loops of sample A and ZnO template measured at 5 K after diamagnetic and paramagnetic subtraction. The sample A exhibits an enhanced ferromagnetism (FM) as compared to the ZnO template and the remanent moment at zero field is $2 \times 10^{-6}$ emu/cm$^2$ after subtracting the contribution from ZnO template. We determine the net spin polarized electrons by adding the net moments of all dipoles in 3DES, yielding $n_S \cdot \zeta = 6.8 \times 10^{11}$ $\mu_B$ cm$^{-2}$ ($\mu_B$ is the Bohr magneton). The net magnetic moment induced by delocalized electrons in 3DES is estimated to be three orders of magnitude lower than the zero-field remanent moment of $1.8 \times 10^{14}$ $\mu_B$ cm$^{-2}$ measured by SQUID. Such a difference is also observed in $LaAlO_3/SrTiO_3$ system[37]. It implied that the host ferromagnetism does not allow spin manipulation and the vast majority of localized spins have no contribution to the transport properties.

So far, the issue of intrinsic ferromagnetism in nonmagnetic oxides nanostructures and thin films is still controversial. Nonetheless, most of the recent reports indicate that the main source of the magnetic moment is likely due to the unpaired 2p electrons at oxygen site surrounding the Zn vacancies, and vacancy-vacancy interaction in the ground state will enhance the magnetic moments[38]. Our XPS and AFM results imply that Zn vacancies are expected to be majority of structural defects at surface regime driven by the polarity stabilization and strain relaxation mechanisms. The theoretical calculation predicted that the surface ferromagnetism in polar ZnO surface is in turn a plausible general stabilization mechanism of polar ionic surfaces[39]. Since Zn vacancies amount are less in the bulk and do not lead to magnetism because of their stronger orbital hybridizations, we believe that Zn vacancies at the surface regime is most likely the main
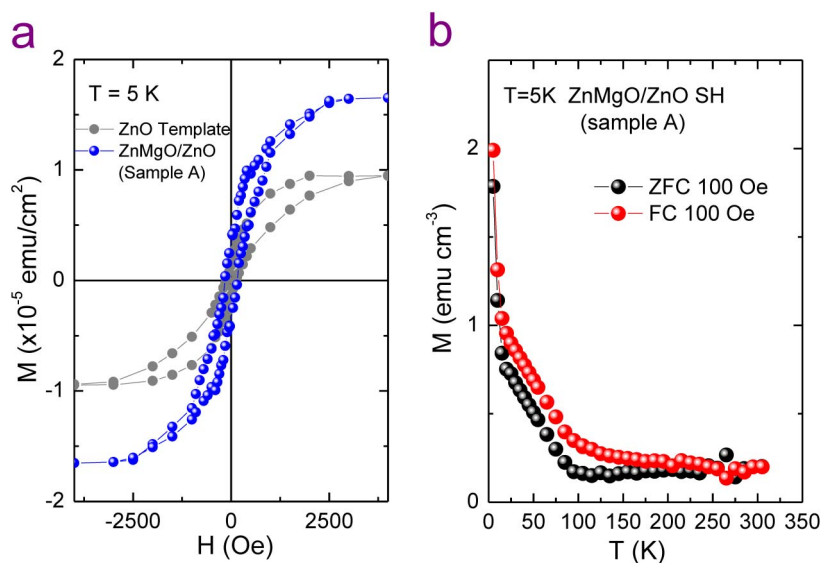


**Figure 8 | (a) The M-H loop after diamagnetic and paramagnetic subtraction for sample A and referenced ZnO template measured at 5 K; (b) zero-field cooled (ZFC) and field-cooled (FC) magnetization curves of sample A.**

source of ferromagnetism. This also agrees with various observations of enhanced ferromagnetism in nanostructured and ultra-thin films in which materials are non-magnetic but exhibit high surface-volume ratio[38]. It was also well supported by the fact that the ferromagnetism is enhanced with the increasing of ZnMgO thickness and Mg composition in a series of controlled samples that we have investigated (see *Supporting Information*).

Figure 8 (b) shows the zero-field cooled (ZFC) and field cooled (FC) magnetization as a function of temperature for sample A. The measurement was carried out while warming the sample from 5 to 300 K using a small applied magnetic field (100 Oe). The magnetization decreases quickly till 90 K and remains weak up to 300 K. The magnitude and temperature dependence of the magnetic response in ZFC and FC curves indicated that the vast majority of the carriers are localized at the surface local moments. Although the valence electrons in O $2p$ orbitals are less delocalized than those in $d$ or $f$ orbitals in transition metals[38], large thermal energy is necessary to activate the electrons localized in such deep level Zn vacancies. Thus, at extreme low temperature, these localized spins are immobile and have no contribution to the transport properties. However, driven by the non-vanishing polarization field across the graded ZnMgO layer, a small fraction of carriers at the surface regime above the Fermi level are migrated and transferred into the conduction band to form 3DES, similar to the transfer process of 2DEG at the LaAlO$_3$/ SrTiO$_3$ and ZnMgO/ZnO interface[26,40]. In this region visited by the itinerant carriers the ferromagnetic exchange interactions are strong via coupling to the surface local moments. The large coherent length and mean free path of electrons also ensure low possibility of spin-flip during carrier migration, thus giving rise to the spin-polarization feature. Note that although $r_s$ in 3DES is not high enough for ferromagnetic phase transition, the diluted electron density definitely favors the spin polarization phenomenon. This is also consistent with small spin polarization degree of 0.35 for the 2DEG confined in ZnMgO/ZnO sharp interface with same Mg composition of $x = 0.18$[15]. Additionally, as the magnetization originates mainly from the surface regime, the interplay of surface charges and spins with the absorbed charged species is expected to be strong, and thus, the ZnO-based open gate transistor can be utilized for biocompatible medicinal applications.

In summary, we have demonstrated the tailoring of polarization effects in functionally graded polar oxides to produce high mobility 3DES without impurity doping. The ability to tune carrier density in graded ZnMgO/ZnO heterostructure provides the opportunity to explore strong correlation effects in the area of quantum transport and spintronics. The important feature of spin polarization is the result of exchanging interaction of itinerant electrons and vacancies induced local magnetic moments. The enhanced correlation effects in such diluted electron system will facilitate the spin polarization, and thus, it could benefit novel all-oxide electronic and spintronic devices for high-field operation.

## Methods

**Sample growth.** ZnMgO/ZnO heterostructures were grown on sapphire (0001) substrates using the Aixtron close-coupled showerhead (CCS) MOVPE system[13]. Dimethylzinc (DMZn) and bis(methlycyclopentadienyl) magnesium (MeCp$_2$Mg) were used as the Zn and Mg sources, respectively. We used N$_2$O as the oxygen source and N$_2$ as the carrier gas. A 0.4 μm-thick ZnO buffer layer was deposited at 450°C, followed by a 3.3 μm undoped ZnO layer and an undoped ZnMgO layer, both grown at 920°C. The ZnO template exhibited a Zn-face polarity with excellent crystal quality and layer-by-layer surface morphology. The values of full-width at half maxima (FWHM) of the ω-scan rocking curves from both symmetric (0002) and asymmetric (10$\bar{1}$1) planes are 186 and 622 arcsec, respectively. It clearly indicates the state-of-the-art quality of the ZnO films with low dislocation density despite of large lattice mismatch (18%) between ZnO and sapphire. The Mg content ($x$) in ZnMgO layer was determined from the reflectance measurement of the bandgap energy of Zn$_{1-x}$Mg$_x$O and using the equation $E_g(x) = E_g(0) + 2.145x$[26].

**Sample characterization.** The surface morphology was characterized by the atomic force microscopy (Nanoscope IIIa, Digital Instruments Inc.) working in the tapping mode and high resolution x-ray diffraction (HRXRD) was performed on a Panalytical

MRD diffractometer equipped with a position sensitive detector placed on the 2θ arm. The Cu K$\alpha$1 radiation was selected by a flat Ge (444) monochromator. Capacitance-voltage (C-V) measurement was performed using mercury contacts at frequency of 1 MHz. Nanoscale analysis was carried out with a monochromated FEI Titan scanning transmission electron microscope (STEM) operated at 300 kV. Energy-dispersive X-ray (EDX) analysis was performed using an electron probe with a relatively large diameter of 0.5 nm to increase the spectral counts. Electron energy-loss spectroscopy (EELS) was further utilized to probe the band structure of the heterostructure using a monochrome STEM probe with a diameter of about 1 nm. The energy resolution of the measurement was better than 0.13 eV and the corrections of bandgap, composition and profiling depth are the same as discussed earlier[41]. Temperature-dependent Hall measurements were carried out at low magnetic field of ~1 T and temperature ranging from 10 to 300 K. Quantum transport properties were measured in a rotator-equipped Oxford refrigerator at 1.4 K with the magnetic field up to 10 T. The field-dependent Hall effect was performed at 10 K for sample A with B field up to 1.4 T. by using the Lakeshore commercial Hall effect system 7707A. Both Hall effect and magnetotransport measurements are performed in a van der Pauw geometry using indium as the ohmic contact metal. The magnetic properties of sample A and ZnO template were measured using superconducting quantum interference devices magnetometry (SQUID) at 5 K. XPS measurements were performed using a Kratos Ultra DLD spectrometer and monochromated Al Kα radiation. The atomic concentrations of each element were determined from the areas of the Zn 2p, Mg 1s, O 1s, and C 1s core-level peaks using sensitivity factors based on spectrometer-modified Scofield cross-sections.

1. Hwang, H. Y., Iwasa, Y., Kawasaki, M., Keimer, B., Nagaosa, N. & Tokura, Y. Emergent phenomena at oxide interfaces. *Nat. Mater.* **11**, 103–113 (2012).
2. Ohtomo, A. & Hwang, H. Y. A high-mobility electron gas at the LaAlO$_3$/SrTiO$_3$ heterointerface. *Nature* **427**, 423–426 (2004).
3. Thiel, S., Hammer, I. G., Schmeh, I. A., Schneider, C. W. & Mannhart, J. Tunable quasi-two-dimensional electron gases in oxide heterostructures. *Science* **313**, 1942–1945 (2006).
4. Tsukazaki, A. *et al.* Quantum hall effect in polar oxide heterostructures. *Science* **315**, 1388 –1391 (2007).
5. Tsukazaki, A. *et al.* Observation of the fractional quantum Hall effect in an oxide. *Nat. Mater.* **9**, 889–893 (2010).
6. Kozuka, Y. *et al.* Single-valley quantum Hall ferromagnet in a dilute Mg$_x$Zn$_{1−x}$O/ZnO strongly correlated two-dimensional electron system. *Phys. Rev. B* **85**, 075302-1–075302-5 (2012).
7. Jena, D., Heikman, S., Green, D., Buttari, D. & Coffie, R. Realization of wide electron slabs by polarization bulk doping in graded III-V nitride semiconductor alloys. *Appl. Phys. Lett.* **81**, 4395–4397 (2002).
8. Simon, J., Protasenko, V., Lian, C. X., Xing, H. L. & Jena, D. Polarization induced hole doping in wide bandgap uniaxial Semiconductor heterostructures. *Science* **327**, 60–64 (2010).
9. Sundaram, M., Allen, S. J. & Gossard, A. C. Low temperature carrier distributions in wide quantum wells of different shapes from capacitance-voltage measurements. *J. Appl. Phys.* **76**, 1003–1007 (1994).
10. Yong, D. P. *et al.* High-temperature weak ferromagnetism in a low-density free-electron. gas. *Nature* **397**, 412–414 (1999).
11. Datta, S. & Das, B. Electronic analog of the electro-optic modulator. *Appl. Phys. Lett* **56**, 665–667 (1990).
12. Hall, C. R. *et al.* Using graded barriers to control the optical properties of ZnO/Zn$_{0.7}$Mg$_{0.3}$O quantum wells with an intrinsic internal electric field. *Appl. Phys. Lett.* **96**, 193117-1–193117-3 (2010).
13. Yoon, J. G., Cho, S. W., Lee, E. & Chung, J. S. Characteristics of indium-tin-oxide Schottky contacts to ZnMgO/ZnO heterojunctions with band gap grading. *Appl. Phys. Lett.* **95**, 222102-1–222102-3 (2009).
14. Rajan, S., DenBaars, S. P., Mishra, U. K., Xing, H. L. & Jena, D. Electron mobility in graded AlGaN alloys. *Appl. Phys. Lett.* **88**, 042103-1–042103-3 (2006).
15. Ye, J. D. *et al.* Two-dimensional electron gas in Zn-polar ZnMgO/ZnO heterostructure grown by metal-organic vapor phase epitaxy. *Appl. Phys. Lett.* **97**, 111908-1–111908-3 (2010).
16. Pereira, S. *et al.* Compositional pulling effects in In$_x$Ga$_{1−x}$N/GaN layers, A combined depth-resolved cathodoluminescence and Rutherford backscattering channelling study. *Phys. Rev. B* **64**, 205311-1–205311-5 (2001).
17. Nishimoto, Y. *et al.* Plasma-assisted molecular beam epitaxy of high optical quality MgZnO films on Zn-polar ZnO substrates. *Appl. Phys. Express* **1**, 091202-1–091202-3 (2008).
18. Matsui, H., Tabata, H., Hasuike, N. & Harima, H. Critical thickness and lattice relaxation of Mg-rich strained Mg$_{0.37}$Zn$_{0.63}$O (0001) layers towards multi-quantum-wells. *J. Appl. Phys.* **99**, 024902-1–024902-7 (2006).
19. Sawai, Y., Hazu, K. & Chivhibu, S. F. Surface stoichiometry and activity control for atomically smooth low dislocation density ZnO and pseudomorphic MgZnO epitaxy on a Zn-polar ZnO substrate by the helicon-wave-excited-plasma sputtering epitaxy method. *J. Appl. Phys.* **108**, 063541-1–063541-8 (2010).
20. Allen, M. W. *et al.* Polarity effects in the x-ray photoemission of ZnO and other wurtzite semiconductors. *Appl. Phys. Lett.* **98**, 101906-1–101906-3 (2011).

21. Dulub, O., Diebold, U. & Kresse, G. Novel stabilization mechanism on polar surface: ZnO(0001)-Zn. *Phys. Rev. Lett.* **90**, 016102-1–016102-4 (2003).
22. Torbrugge, S., Ostendorf, F. & Reichling, M. Stabilization of Zinc-terminated ZnO (0001) by a modified surface stoichiometry. *J. Phys. Chem. C* **113**, 4909–4914 (2009).
23. Lai, J. H. *et al.* Stabilization of ZnO polar plane with charged surface nanodefects. *Phys. Rev. B* **82**, 155406-1–155406-5 (2010).
24. Snider, G. L. *1D Poisson*, URL, http//www.nd.edu/~gsnider/
25. Furno, E. *et al.* Electronic and optical properties of $Mg_xZn_{1-x}O$ and $Be_xZn_{1-x}O$ quantum wells. *J. Electron. Mater.* **39**, 936–942 (2010).
26. Tampo, H. *et al.* Polarization-induced two-dimensional electron gases in ZnMgO/ ZnO heterostructures. *Appl. Phys. Lett.* **93**, 202104-1–202104-3 (2008).
27. Wang, X. F. *et al.* Terahertz time-domain magnetospectroscopy of a high-mobility two-dimensional electron gas. *Opt. Lett* **32**, 1845–1847 (2007).
28. Jena, D., Gossard, A. C. & Mishra, U. K. Dipole scattering in polarization induced III–V nitride two-dimensional electron gases. *J. Appl. Phys.* **88**, 4734–4738 (2000).
29. Murzin, S. S., Jansen, A. G. M. & Linden, P. Quantization of the Hall Conductance in a three-dimensional layer. *Phys. Rev. Lett.* **80**, 2681–2684 (1998).
30. Zeng, Y. J. *et al.* Tuning quantum corrections and magnetoresistance in ZnO nanowires by ion implantation. *Nano Lett.* **12**, 666–672 (2012).
31. Sergio, C. S. *et al.* Coexistence of a two- and three-dimensional Landau states in a wide parabolic quantum well. *Phys. Rev. B* **64**, 115314-1–115314-9 (2001).
32. Smith, J. L. & Stiles, P. J. Electron-Electron Interactions Continuously Variable in the Range $2.1 > r_s > 0.9$. *Phys. Rev. Lett.* **29**, 102–104 (1972).
33. Yan Voon, L. C., Willatzen, M., Cardona, M. & Christensen, N. E. Terms linear in k in the band structure of wurtzite-type semiconductors. *Phys. Rev. B* **53**, 10703–10714 (1996).
34. Shalom, M., Tai, C. W., Lereah, Y., Sachs, M. & Levy, E. Anisotropic magnetotransport at the SrTiO₃/LaAlO₃ interface. *Phys. Rev. B* **80**, 140403-1–140403-4 (2009).
35. Brinkman, A., Huigben, M., Zalk, M. V., Huijben, J. & Zeitler, U. Magnetic effects at the interface between non-magnetic oxides. *Nat. Mater.* **6**, 493–496 (2007).
36. Zong, F. H., Lin, C. & Ceperley, D. M. Spin polarization of the low-density three-dimensional electron gas. *Phys. Rev. E* **66**, 036703-1–036703-7 (2002).
37. Bert, J. A. *et al.* Direct imaging of the coexistence of ferromagnetism and superconductivity at the LaAlO₃/SrTiO₃ interface. *Nat. Phys.* **7**, 767–771 (2011).
38. Wang, Q., Sun, Q., Chen, G., Kawazoe, Y. & Jena, P. Vacancy-induced magnetism in ZnO thin film and nanowires. *Phys. Rev. B* **77**, 205411-1–205411-7 (2008).
39. Fischer, G. *et al.* Room-temperature p-induced surface ferromagnetism: First-princiles study. *Phys. Rev. B* **84**, 205306-1–205306-5 (2011).
40. Yoshimatsu, K., Yasuhara, R., Kumigashira, H. & Oshima, M. Origin of metallic states at the heterointerface between the band insulators LaAlO₃ and SrTiO₃. *Phys. Rev. Lett* **101**, 026802-1–026802-4 (2008).
41. Bosman, M. *et al.* Nanoscale band gap spectroscopy on ZnO and GaN-based compounds with a monochromated electron microscope. *Appl. Phys. Lett.* **95**, 101110-1–101110-3 (2009).

## Acknowledgements

## Author contributions

M. B. carried out the TEM and EELS experiments; S. L. G. and Y. D. Z. performed Hall measurement; S. T. L. carried out the magnetotransport, XPS and SQUID experiments; J. D. Y. and K. L. T. designed the research, carried out all the experiments, analysed the data and co-wrote the manuscript, which H. H. T., C. J. and X.W. S. edited. All authors discussed the results and commented on the manuscript.

## Additional information

**How to cite this article:** Ye, J. *et al.* Spin-polarized Wide Electron Slabs in Functionally Graded Polar Oxide Heterostructures. *Sci. Rep.* **2**, 533; DOI:10.1038/srep00533 (2012).